NANO · MICRO small
www.small-journal.com

Formation of B—N—C Coordination to Stabilize the Exposed Active Nitrogen Atoms in g-C_3N_4 for Dramatically Enhanced Photocatalytic Ammonia Synthesis Performance

Weikang Wang, Hongjian Zhou, Yanyan Liu, Shengbo Zhang, Yunxia Zhang, Guozhong Wang, Haimin Zhang, and Huijun Zhao**

It is an important issue that exposed active nitrogen atoms (e.g., edge or amino N atoms) in graphitic carbon nitride (g-C_3N_4) could participate in ammonia (NH_3) synthesis during the photocatalytic nitrogen reduction reaction (NRR). Herein, the experimental results in this work demonstrate that the exposed active N atoms in g-C_3N_4 nanosheets can indeed be hydrogenated and contribute to NH_3 synthesis during the visible-light photocatalytic NRR. However, these exposed N atoms can be firmly stabilized through forming B—N—C coordination by means of B-doping in g-C_3N_4 nanosheets (BCN) with a B-doping content of 13.8 wt%. Moreover, the formed B—N—C coordination in g-C_3N_4 not only effectively enhances the visible-light harvesting and suppresses the recombination of photogenerated carriers in g-C_3N_4, but also acts as the catalytic active site for N_2 adsorption, activation, and hydrogenation. Consequently, the as-synthesized BCN exhibits high visible-light-driven photocatalytic NRR activity, affording an NH_3 yield rate of 313.9 µmol g^{-1} h^{-1}, nearly 10 times of that for pristine g-C_3N_4. This work would be helpful for designing and developing high-efficiency metal-free NRR catalysts for visible-light-driven photocatalytic NH_3 synthesis.

1. Introduction

It is well known that nitrogen (N_2) accounts for ≈78% in our atmospheric environment, which is essential element for almost all life forms including plants and animals on earth. Up to now, the most mature technology of artificial synthetic ammonia (NH_3) is the over century-old Haber–Bosch process, operated under drastic conditions due to the intrinsically inert characteristic of N_2 molecules.[1,2] More seriously, the industrial Haber–Bosch process consumes nearly 2% of the world annual energy supply and produces more than 2 tons of CO_2 per year.[3,4] Due to wide applications of NH_3 product in chemical synthesis industry, the development of energy-efficient and ambient NH_3 synthesis technology through fixation of atmospheric N_2 is highly desirable, but great challenging.[5–7]

Currently, photo(electro)catalytic N_2 reduction has been regarded as a promising means for sustainable NH_3 synthesis at ambient conditions.[6–8] To date, varieties of catalysts, including BiOBr nanosheets, MXene-derived TiO_2@C/g-C_3N_4, gold nanoparticles/black Si/Cr and other catalysts,[3,9–12] have been developed and investigated for photo(electro)catalytic nitrogen reduction reaction (NRR), indicating high catalytic performance. As a class of metal-free polymer semiconductor photocatalyst, graphitic carbon nitride (g-C_3N_4) possesses many advantages,[13] such as low cost, abundance, superior visible-light activity and high chemical/photochemical stability, exhibiting great potential for photocatalytic NRR.[5,14] However, several issues are still existent associated with the NRR using the g-C_3N_4-based photocatalyst: i) If the exposed active N atoms (e.g., edge or amino N atoms) in g-C_3N_4 will participate in the hydrogenation reaction during photocatalytic NRR, thus contributing the NH_3 formation?[15] ii) If these N atoms can participate in the NH_3 formation during photocatalytic NRR, are there effective ways to stabilize them, and concurrently endow new catalytic active sites for N_2 adsorption, activation, and hydrogenation? iii) The pristine bulk g-C_3N_4 generally possesses relative low specific surface area, which is adverse to the N_2 adsorption and activation, as well as high recombination rate of photogenerated electrons and holes, resulting in its low photocatalytic efficiency.[16] Based on the above discussions, developing effective strategies to achieve high-efficiency g-C_3N_4-based photocatalyst, capable of improving the N_2 adsorption/activation and visible-light

W. Wang, Dr. H. Zhou, Y. Liu, S. Zhang, Prof. Y. Zhang, Prof. G. Wang, Prof. H. Zhang, Prof. H. Zhao
Key Laboratory of Materials Physics
Centre for Environmental and Energy Nanomaterials
Anhui Key Laboratory of Nanomaterials and Nanotechnology
CAS Center for Excellence in Nanoscience
Institute of Solid State Physics
Chinese Academy of Sciences
Hefei, Anhui 230031, China
E-mail: zhanghm@issp.ac.cn

W. Wang, Y. Liu, S. Zhang
Science Island Branch of Graduate School
University of Science and Technology of China
Hefei, Anhui 230026, China

Prof. H. Zhao
Centre for Clean Environment and Energy
Griffith University
Gold Coast Campus, Queensland 4222, Australia
E-mail: h.zhao@griffth.edu.au

The ORCID identification number(s) for the author(s) of this article can be found under https://doi.org/10.1002/smll.201906880.

DOI: 10.1002/smll.201906880

utilization, simultaneously effectively inhibiting the recombination of photogenerated carriers in g-C_3N_4, is critically important and highly needed. Recently, Shiraishi and co-workers have demonstrated that heteroatom doping could be an effective means to regulate the electronic structures of g-C_3N_4, thus obtaining new catalytic active sites (N vacancy) for N_2 adsorption and activation, leading to an high-efficiency NH_3 synthesis performance.[17] More importantly, Wang et al. theoretically predicted that B-doping in g-C_3N_4 can not only improve the visible-light utilization efficiency, also reaching rather low onset potential for photocatalytic NRR based on the concept of electron "acceptance–donation" on B atoms, similar to that of transition metals.[5,18] Furthermore, as a p-type doping, the incorporation of B atoms in g-C_3N_4 can also construct a nanoscale p–n heterojunction structure, leading to more effective charge separation for high-efficiency photocatalysis.[19,20] Besides of the above-mentioned advantages, the formation of B−N−C coordination in B-doped g-C_3N_4 can be an effective approach to immobilize the exposed active N atoms in g-C_3N_4. This approach possibly means that no NH_3 product resulted from the exposed active N atoms in g-C_3N_4 can be detected during photocatalytic NRR. However, the related studies have not been reported in literatures.

Herein, the porous B-doped g-C_3N_4 nanosheets (BCN) were synthesized by a facile thermal treatment approach using dicyandiamide (DICY) and boron oxide (B_2O_3) as reactants. The resultant BCN with a B-doping content of 13.8 wt% displays a porous structure with a large surface area of 123 m^2 g^{-1}. As photocatalyst under visible-light irradiation (wavelength of >400 nm) using 1.0×10^{-3} M Na_2SO_3 as hole sacrifice agent, the BCN shows high photocatalytic activity toward NRR, affording an NH_3 yield rate of 313.9 μmol g^{-1} h^{-1}, which is comparable to most of recently reported NRR photocatalysts (Table S1, Supporting Information). Interestingly, it was found that an NH_3 yield rate of 16.7 μmol g^{-1} h^{-1} can be achieved for the pristine g-C_3N_4 photocatalyst in Ar-saturated Na_2SO_3 solution under visible-light irradiation, while an ignorable NH_3 yield can be obtainable for the BCN under the identical experimental conditions. These can be further confirmed by the isotopic labeling experiment results. The above results indicate that some exposed active N atoms in g-C_3N_4 can indeed participate in the NH_3 formation during the photocatalytic NRR, which can be firmly stabilized by forming B−N−C bonds in BCN. Moreover, the B-doping in g-C_3N_4 can effectively regulate its electronic structure, thus facilitating the visible-light utilization and inhibiting the recombination of photogenerated carriers, meanwhile act as the catalytic active sites for N_2 adsorption and activation, resulting in dramatically enhanced photocatalytic NRR performance.

2. Results and Discussion

In this work, the BCN was synthesized by a facile thermal treatment approach. For comparison, the g-C_3N_4 nanosheets (CN) without B-doping were also fabricated. **Figure 1**a shows the X-ray diffraction (XRD) patterns of BCN and CN samples, revealing typical (100) in-plane structural packing of heptazine system at 13.1° and (002) interlayer-stacking diffraction peak at 27.7° for both two samples.[21] Obviously, it was found that the (002) peak of BCN shifts slightly toward low angle compared to that of CN, moreover, the (100) and (002) peak intensities of BCN are obviously decreased, possibly suggesting that B atoms are successfully doped into the g-C_3N_4 framework. Figure S1 (Supporting Information) shows the field-emission scanning electron microscope (FE-SEM) images of CN and BCN. In comparison with CN, the BCN sample displays more loose structure morphology, possibly meaning its larger surface area. The transmission electron microscopy (TEM) images (Figure 1b,c) indicate that the CN sample shows a typical 2D sheet-like structure, while the BCN displays more fluffy foam-like porous structure. The above results suggest that B-doping treatment results in more abundant porous structure of carbon nitride nanosheets, favorable for providing more catalytic active sites and facilitating mass transport for high-efficiency photocatalysis.[22] Additionally, both nitrogen (N_2) adsorption–desorption isotherms (Figure 1d) of BCN and CN samples demonstrate a type IV isotherm with H3-type hysteresis loop,[23] illustrating their porous characteristics. The pore diameter distribution curves (inset of Figure 1d) reveal a relatively wide pore distribution ranging from 5.0 to 100 nm for BCN, meaning the existence of bimodal pore structure including mesopores (≈7.0 nm) and macropores (>50 nm), while the CN sample only shows a pore size distribution centered at ≈50 nm. As a result, the BCN exhibits larger surface area of 123 m^2 g^{-1} than that of CN (48 m^2 g^{-1}). The large surface area and porous structure of BCN are favorable for exposing more catalytic active sites and enhancing mass transport for high-efficiency photocatalysis.

To confirm the successful doping of B atoms in g-C_3N_4 nanosheets, we further performed the Fourier-transform infrared spectroscopy (FT-IR) and X-ray photoelectron spectroscopy (XPS) characterizations. As shown in Figure S2a (Supporting Information), the CN sample exhibits typical N−H stretching vibrations, C−N heterocycle stretching vibration and out-of-plane bending vibration of heptazine rings for g-C_3N_4.[16,24] Comparatively, the typical B−N vibration at ≈1370 cm^{-1} can be observed for the BCN, as well as the bands at 920 cm^{-1} are ascribed to the B−N−C species formed in BCN.[25–27] After B-doping, the intensities of C−N heterocycle vibration peaks of the BCN are obviously decreased compared to CN, mainly due to the change of C−N lattice structure resulted from B-doping.[19] Figure S2b (Supporting Information) exhibits the surface XPS full spectra of CN and BCN samples. Both tested samples contain C, N, and O elements, while B element can be only detected for the BCN with a B-doping content of 13.8 wt%. In the high-resolution C 1s spectrum (**Figure 2**a) of BCN, no peak at binding energy of ≈283.0 eV can be found, ruling out the formation of B−C bonds in g-C_3N_4.[28,29] In comparison with CN, the C 1s peaks of N = C−N in BCN obviously shift toward high binding energy by ≈0.2 eV. This is mainly owing to the extranuclear electrons deviated to B−N pairs induced by B-doping (a typical p-type doping with less outermost electron) in g-C_3N_4.[28,30] Indeed, the relative intensity of peak area for N = C−N decreased, resulting from a certain amount of C replaced by B atoms. In addition, the high-resolution N 1s spectrum (Figure 2b) of BCN shows that the peaks of bicoordinated (C−N = C) and tricoordinated ($N-(C)_3$) nitrogen atoms are still maintained well, meaning no

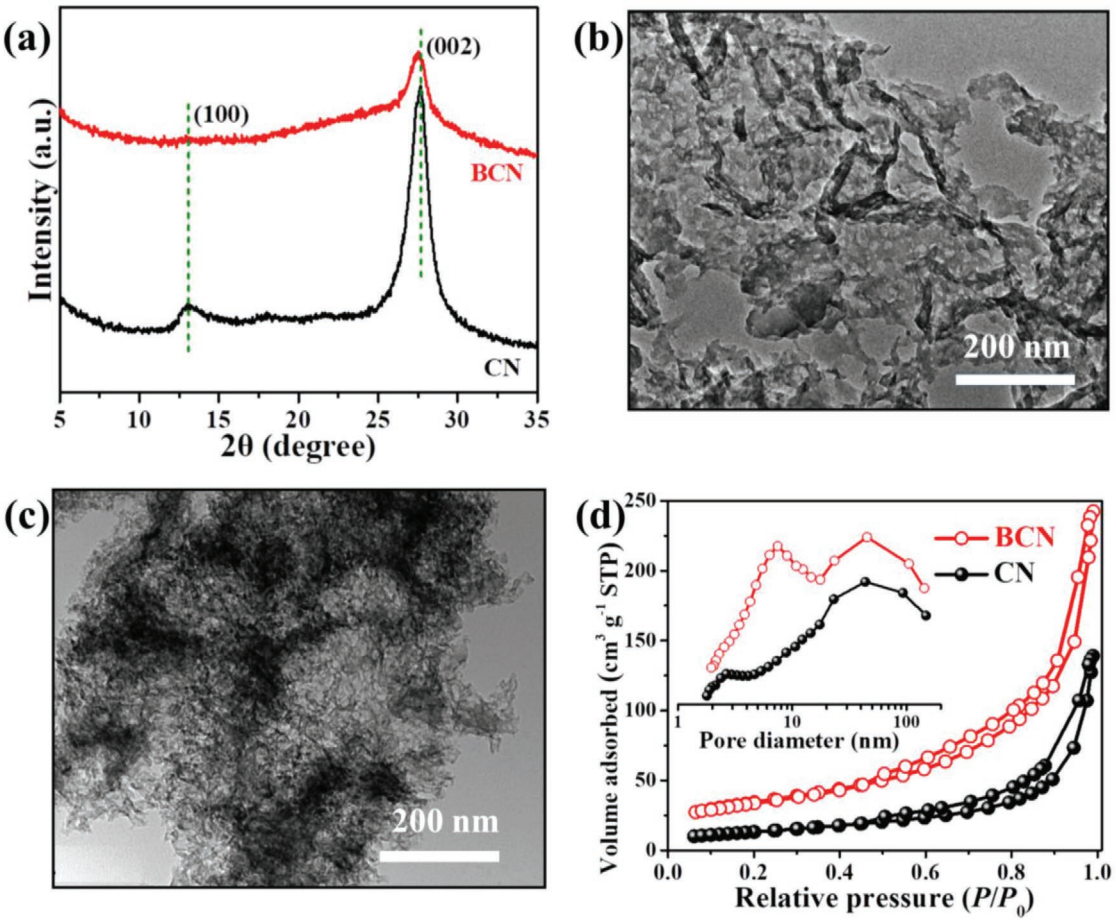

Figure 1. a) XRD patterns, b,c) TEM images, and d) N_2 adsorption–desorption isotherms and corresponding pore size distribution curves (inset) of CN and BCN samples.

significant structural change of g-C_3N_4 for BCN. However, the relative amount of C—N = C decreased as the B—N—C bonds constructed with B-doping, and the binding energy of tricoordinated N atoms declined by ≈0.1 eV due to N—$(C)_3$ in heptazine rings capturing more electrons when the B atoms doping in bay sites.[25] Importantly, the N 1s peak of —NH_x disappeared, because it can react with B_2O_3 (Figure S3, Supporting Information), which increases the thermal stability of g-C_3N_4.[31] The above results suggested that B-doping can effectively stabilize the exposed active N atoms in g-C_3N_4. Additionally, the peak at binding energy of ≈398.0 eV can be observed for the BCN, assigned to the C—N—B bond,[27–29] consistent with the FT-IR results. In Figure 2c, the peaks in high-resolution B 1s spectrum of BCN are mainly concentrated at ≈192.2 and ≈191.5 eV, ascribed to the formed B-$(N)_3$ and —N_2BH bond, respectively.[25,31] The solid-state ^{11}B nuclear magnetic resonance (SSNMR) spectrum (Figure 2d) of BCN further confirms this. The NMR spectrum of BCN reveals a dominant broad signal peak at 10.1 ppm, a sharp signal peak at 0.9 ppm, and a small one at -4.2 ppm, attributed to the B-doping in the corner- and bay-carbon sites (including sp^3-coordinated borane such as —N_2BH, inset of Figure 2d) of heptazine rings in g-C_3N_4.[25,29,31] Moreover, no B—C or B—B signal peak is detectable, indicating the doping of B atoms atomically dispersed in the g-C_3N_4 framework, mainly in the bay- and corner-carbon sites to form B—N—C coordination (Figure S3, Supporting Information). The formed B—N—C coordination possibly plays important role in stabilizing the exposed active N atoms in g-C_3N_4, and concurrently provides new catalytic active sites for N_2 adsorption and activation.[5]

As expected, the B-doping in g-C_3N_4 can optimize its interlayer/in-plane structures, thus regulating the optical/electronic properties of g-C_3N_4.[31,32] **Figure 3**a shows the UV–vis diffuse reflectance spectra (DRS) of CN and BCN samples. Compared with the CN, the BCN exhibits a strong tail absorption (also called urbach tail) in the visible-light range, mainly due to the localized electronic states located in bandgap resulted from the B-doping. Consequently, the optical absorption edge of BCN displays an obvious redshift with a bandgap of ≈2.50 eV compared to CN with a bandgap of ≈2.76 eV, based on the Tauc plots $(\alpha h\upsilon)^2$ (Figure S4, Supporting Information). The BCN with a narrowed bandgap is very favorable for visible-light utilization, thus improving the photocatalytic performance. Figure 3b exhibits the steady-state photoluminescence (PL) spectra of CN and BCN samples, indicating dramatically decreased PL intensity of BCN compared to CN. This means that the B-doping in g-C_3N_4 can effectively inhibit the recombination of photogenerated electron–hole pairs due to the formed built-in electrical field by

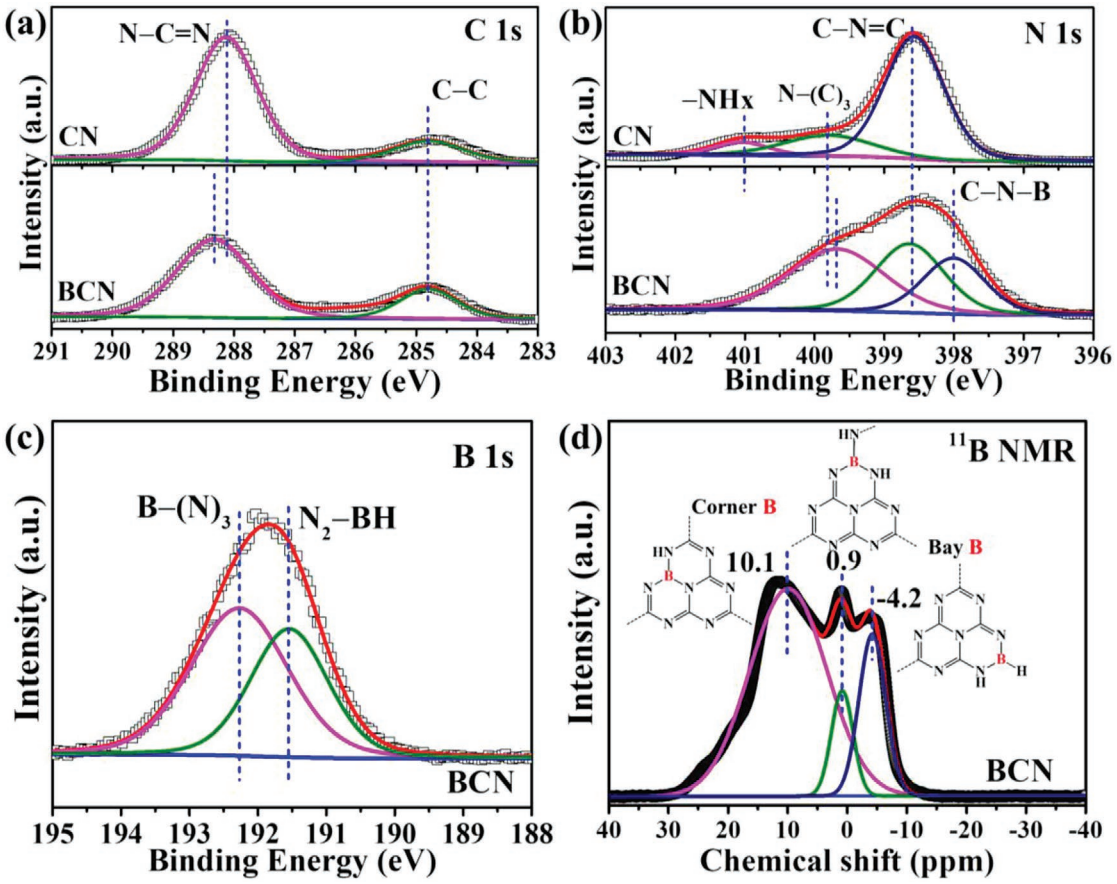

Figure 2. a) High-resolution C 1s and b) N 1s XPS spectra of CN and BCN. c) High-resolution B 1s spectra and d) ^{11}B SSNMR spectra of BCN (inset of the inferred g-C_3N_4 unit with different B-doping sites).

p–n junction,[19,32] favorable for enhancing the photocatalytic efficiency. The Mott–Schottky (M-S) analysis was subsequently conducted to identify the conductivity types of the samples. As shown in Figure S5a,b (Supporting Information), the curve with combined positive with negative slopes located in different potential regions was achieved for the BCN at a fixed frequency, while the M-S curve of CN sample only shows the positive slope. The above results reveal that the CN is a typical n-type semiconductor, while the co-existence of n- and p-type semiconductor in the BCN is mainly ascribed to the p-type doping of B atoms in g-C_3N_4. The resultant p–n junction can construct a built-in electrical field, favorable for the high-efficiency separation of the photogenerated electron–hole pairs, responsible for the decreased PL intensity of BCN.[32] Figure 3c shows the transient photocurrent curves of CN and BCN photocatalysts under irradiation of 250 W Xe lamp with a cut-off filter ($\lambda > 400$ nm, light intensity of 0.5 W cm^{-2}), demonstrating that under the identical conditions, the transient photocurrent density of BCN photocatalyst is obviously higher than that of CN photocatalyst. Additionally, it can be observed clearly that the photocurrent curve of BCN reveals a slow-rising trend, and finally reaches a higher level than that of CN. This phenomenon can be ascribed to that a built-in electrical field forms in BCN when the light turns on, which efficiently suppresses the photogenerated charge recombination and boosts the charge transfer, thus improving the photocatalytic efficiency.[33]

As we know, the g-C_3N_4-based photocatalysts and electrocatalysts have recently demonstrated high catalytic activity toward the NRR to NH_3 at ambient conditions.[7,9,34] However, owing to abundant N atoms contained in g-C_3N_4, a still concerned issue associated with the NRR is if the exposed active N (e.g., edge or amino N) atoms in g-C_3N_4 catalysts would be hydrogenated and participant in the formation of NH_3. For this, we subsequently investigated the photocatalytic NRR activities of BCN and CN catalysts using 1.0×10^{-3} M Na_2SO_3 solution as hole sacrifice agent under visible-light irradiation ($\lambda > 400$ nm, 250 W Xe lamp, 0.5 W cm^{-2}). To eliminate the interferences of possible NH_3 and NO_x (including NO and NO_2) from environment toward the NH_3 synthesis by photocatalytic NRR, the used N_2 (or Ar) feeding gas was first pre-purified using 0.01 M H_2SO_4 solution and deionized (DI) water, and the N_2 (or Ar) tail gas passing through the photocatalytic reactor was absorbed by two sequential 0.01 M H_2SO_4 solution to avoid the NH_3 loss, as shown in Figure S6 (Supporting Information). Prior to photocatalytic NRR test, the possible presence of NO_x in the feeding gases ($^{14}N_2$ and $^{15}N_2$) can be excluded by the ion chromatography results collected after blowing the feeding gas through a CrO_3 catalyst tube (converting possible NO to soluble NO_2) into the Na_2SO_3 solution (1.0×10^{-3} M) for 3 h, confirming the absence of NO_x in both gases (Figure S7, Supporting Information).[35]

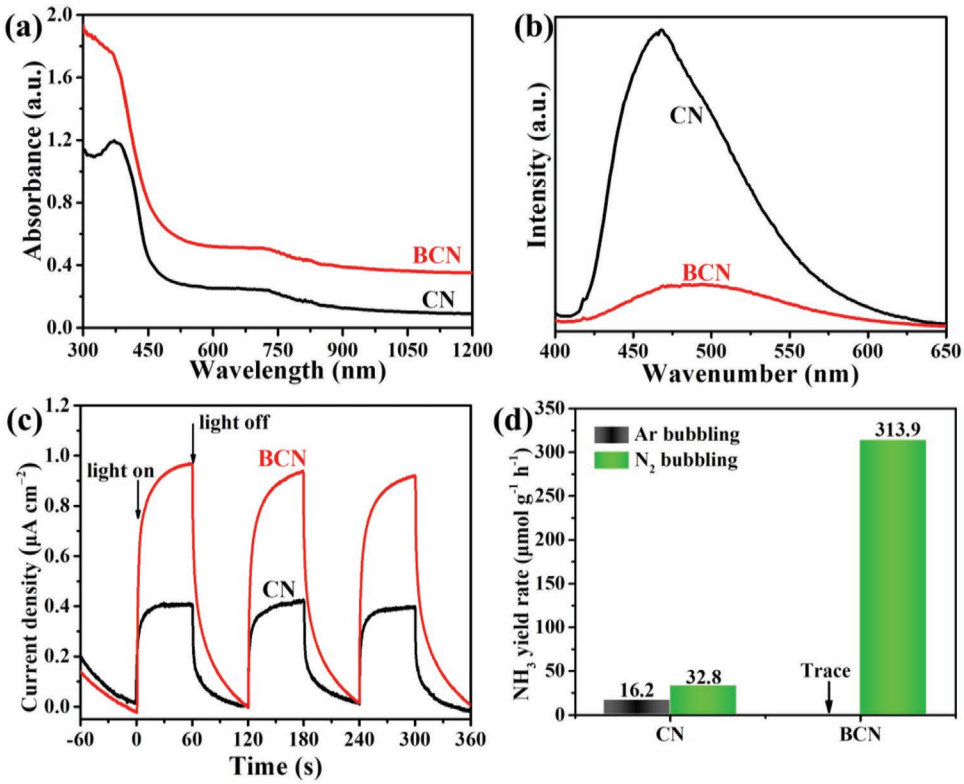

Figure 3. a) UV–vis DRS spectra, b) steady-state PL spectra, c) transient photocurrent responses, and d) photocatalytic NH_3 yield rates of CN and BCN photocatalysts.

Using this reliable photocatalytic reaction system, the photocatalytic NRR of CN and BCN catalysts was conducted in Ar- and N_2-saturated Na_2SO_3 solution under visible-light irradiation. The obtained NH_3 product from photocatalytic NRR of these two catalysts was qualitatively and quantitatively analyzed by the Nessler's reagent colorimetric method (Figure S8, Supporting Information).[6,36] The preliminary experimental results demonstrate that the produced NH_3 is merely existent in the Na_2SO_3 solution in photocatalytic reactor, undetectable in the tail gas absorption solution (0.01 M H_2SO_4 solution) for both two photocatalysts. Interestingly, it was found that with 3 h of visible-light irradiation in Ar-saturated Na_2SO_3 solution, the produced NH_3 by CN photocatalyst (40 mg) can be detected with a yield rate of 16.7 μmol g^{-1} h^{-1}, while the NH_3 yield rate is obviously increased to 32.8 μmol g^{-1} h^{-1} in N_2-saturated Na_2SO_3 solution (Figure 3d). The above results indicate that the active *H/electron pair could attack the exposed active N atoms (e.g., edge or amino N atoms) in CN catalyst, resulting in their hydrogenation to form NH_3 in Ar-saturated Na_2SO_3 solution during photocatalytic NRR. This means that the exposed active N atoms in CN readily break away from the catalyst surface to contribute NH_3 synthesis under visible-light irradiation. However, the NH_3 yield rate enhancement of CN catalyst in N_2-saturated Na_2SO_3 solution under visible-light irradiation can be ascribed to the generated N vacancies in CN catalyst as the catalytic active sites for further adsorption, activation, and hydrogenation of N_2 molecules.[34,37] To further identify this assumption, the FT-IR spectra of CN and BCN were collected after photocatalytic NRR with Ar as feeding gas (denoted as CN- and BCN-used in Figure S9, Supporting Information). It reveals no obvious difference between the FT-IR spectra of BCN before and after photocatalytic NRR in Ar-saturated Na_2SO_3 solution. However, compared with that of fresh CN sample, the broad absorption bands from 3000 to 3400 cm^{-1} derived from various vibration modes of the N—H_x ($x = 1$ or 2) bonds in CN-used are basically disappeared,[24] owing to the exposed —NH_x groups to accept the photogenerated H^+/electron pairs and form NH_3 molecule.

Using similar experimental procedures, we subsequently evaluated the photocatalytic NRR activity of BCN catalyst. Importantly, it can be found in Figure S10 (Supporting Information) that no measureable NH_3 product can be detected using BCN photocatalyst in Ar-saturated 1.0×10^{-3} M Na_2SO_3 solution under visible-light irradiation. The above result suggests that the N element contained in BCN catalyst cannot contribute the NH_3 synthesis, meaning that the surface exposed active N atoms in CN structure can be firmly anchored by forming stable B—N—C coordination. In N_2-saturated 1.0×10^{-3} M Na_2SO_3 solution with visible-light irradiation of 2 h, the BCN exhibits an NH_3 yield rate of 313.9 μmol g^{-1} h^{-1}, significantly higher than that of the CN catalyst (32.8 μmol g^{-1} h^{-1}). The NH_3 synthesis performance of BCN in this work is comparable with most of recently reported photocatalytic NRR catalysts (Table S1, Supporting Information). Moreover, it can be observed in Figure S11 (Supporting Information) that the quantum efficiency (QE) for NH_3 synthesis by BCN under near monochromatic light irradiation (420, 450, 500, 550, 600, and 650 nm) closely fits the absorption spectrum of the photocatalyst, with the optimal QE determined to be nearly 0.64% at 420 nm.

To clarify the effect of N-defects (such as N vacancy) on the photocatalytic NRR performance, the electron paramagnetic resonance (EPR) spectra of both CN and BCN were obtained (Figure S12, Supporting Information), demonstrating the Lorentzian lines of CN and BCN, where the Lande factor (g) is calculated using $g = 0.07145*\gamma(\text{MHz})/H(\text{mT})$, ($\gamma$: microwave frequency and H: magnetic field strength). Both Lorentzian lines are found to be centered at an essentially same g value (2.002), demonstrating the same type of unpaired electrons on the π-conjugated g-C_3N_4 aromatic rings are generated from both CN and BCN.[15] As expected, the EPR intensity of BCN reveals a little less than that of pristine CN, indicating that the concentration of N-defects (including N vacancy) of g-C_3N_4 decreased slightly after B-doping. This result further confirms that the enhanced photocatalytic NRR performance is mainly attributed to the B atoms doping in the g-C_3N_4.

The above experimental results indicate that the formation of B—N—C bonds not only effectively stabilizes the surface exposed active N atoms in CN structure, but also boosts the photocatalytic performance.[5,32] Similarly, ignorable NH_3 product is detectable in N_2-saturated 1.0×10^{-3} M Na_2SO_3 solution with BCN catalyst in dark condition as revealed in Figure S10 (Supporting Information), indicating the yielded NH_3 is from the photocatalytic NRR process catalyzed by the BCN catalyst.

To further confirm the validity of the above experimental results, the isotope labeling experiments were also carried out using $^{14}N_2$ and $^{15}N_2$ as the feeding gases in 1.0×10^{-3} M Na_2SO_3 solution with or without light irradiation. Prior to all experiments, the used $^{14}N_2$ and $^{15}N_2$ feeding gases were also pre-purified using 0.01 M H_2SO_4 solution and DI water to eliminate environmental NH_3 interferences.[38] Then, we analyzed the ^{1}H NMR spectra[12,39] of photocatalytic reaction solution collected after several control experiments conducted in Ar-saturated 1.0×10^{-3} M Na_2SO_3 solution using CN and BCN catalysts with or without visible-light irradiation for 3 h to determine trace amount of NH_3 product. **Figure 4**a indicates that an ignorable NH_3 product is detectable for both photocatalysts without visible-light irradiation (denoted as dark condition). Under visible-light irradiation, the ^{1}H NMR spectrum of the sample obtained in Ar-saturated Na_2SO_3 solution using CN catalyst exhibits typical triple peaks of ^{14}N for $^{14}NH_4^+$, confirming that the surface exposed active N atoms in CN structure indeed contribute the NH_3 synthesis with a yield rate of 16.7 μmol g^{-1} h^{-1} by the quantitative analysis of ^{1}H NMR spectrum (Figure S13, Supporting Information). However, the ^{1}H NMR spectrum of the sample obtained in Ar-saturated Na_2SO_3 solution using BCN catalyst under visible-light irradiation shows undetected triple peaks of ^{14}N for $^{14}NH_4^+$, indicating the formation of ignorable NH_3 product. This also means that after B-doping in CN, the exposed active N atoms in CN structure can be firmly stabilized by the formed B—N—C bonds.

Subsequently, the ^{1}H NMR analysis was also carried out to quantitatively confirm the yielded NH_3 exclusively derived from the BCN catalyzed NRR under visible-light irradiation. The experiments were carried out using $^{14}N_2$ and $^{15}N_2$ as the feeding gases in Na_2SO_3 solution with BCN catalyst under visible-light irradiation for 2 h. Figure 4b shows the ^{1}H NMR spectra of the standards and the yielded $^{14}NH_4^+$ and $^{15}NH_4^+$. The concentration of yielded $^{14}NH_4^+$ and $^{15}NH_4^+$ in reaction solution after photocatalytic NRR analyzed by ^{1}H NMR is 0.56 and 0.58 μmol mL^{-1}, respectively, almost identical to the determined values (0.60 μmol mL^{-1} of $^{14}NH_4^+$ and 0.62 μmol mL^{-1} of $^{15}NH_4^+$) from the Nessler's reagent colorimetric method. The almost identical $^{14}NH_4^+$ and $^{15}NH_4^+$ concentrations determined by both methods categorically confirm that the yielded NH_3 is exclusively resulted from the BCN catalyzed NRR.

Several recent theoretical calculations studies reveal that B-doping can effectively regulate the electronic structure of g-C_3N_4, thus facilitating the photocatalytic NRR activity for high-efficiency NH_3 production.[5,40] Moreover, B sites (or B—N pairs) have been proven to be the catalytic active sites for N_2 adsorption and activation.[8,41,42] In this work, the nitrogen temperature programmed desorption (N_2-TPD) measurements were performed to experimentally confirm the N_2 adsorption on B—N—C active sites in g-C_3N_4. As the chemisorption of N_2 on an photo(electro)catalyst is a pre-requisite of NRR process,[3,37,42] such B-doping in BCN induces a strong N_2 adsorption on B active sites (**Figure 5**a), which could be an important attributor for the enhanced photocatalytic NRR performance. This significantly improved N_2 adsorption on BCN can be further identified by the molecular dynamics (MD) simulations.[43] The snapshots (Figure 5b,c) obtained at the same time, demonstrate an obvious distinction of the two models for CN and

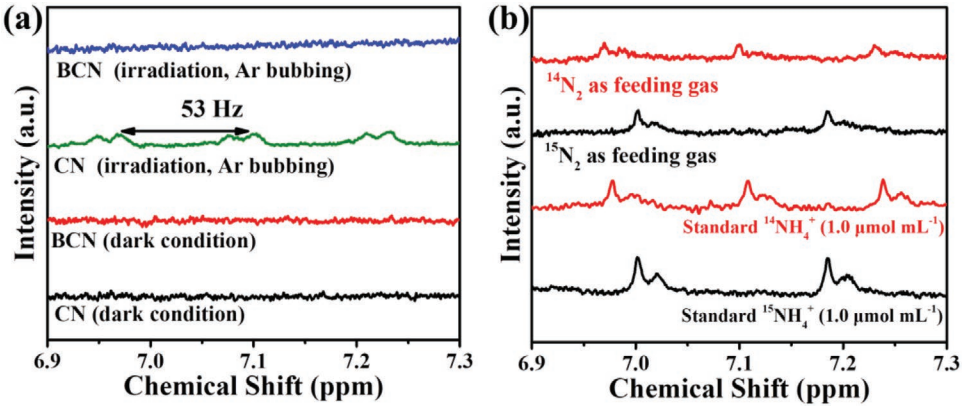

Figure 4. a) ^{1}H NMR spectra of CN and BCN in Na_2SO_3 solution under dark condition or irradiation with Ar bubbing. b) ^{1}H NMR spectra of photocatalytic yielded $^{14}NH_4^+$ or $^{15}NH_4^+$ from $^{14}N_2$ and $^{15}N_2$ feeding gases, and corresponding standards (1.0 μmol mL^{-1}).

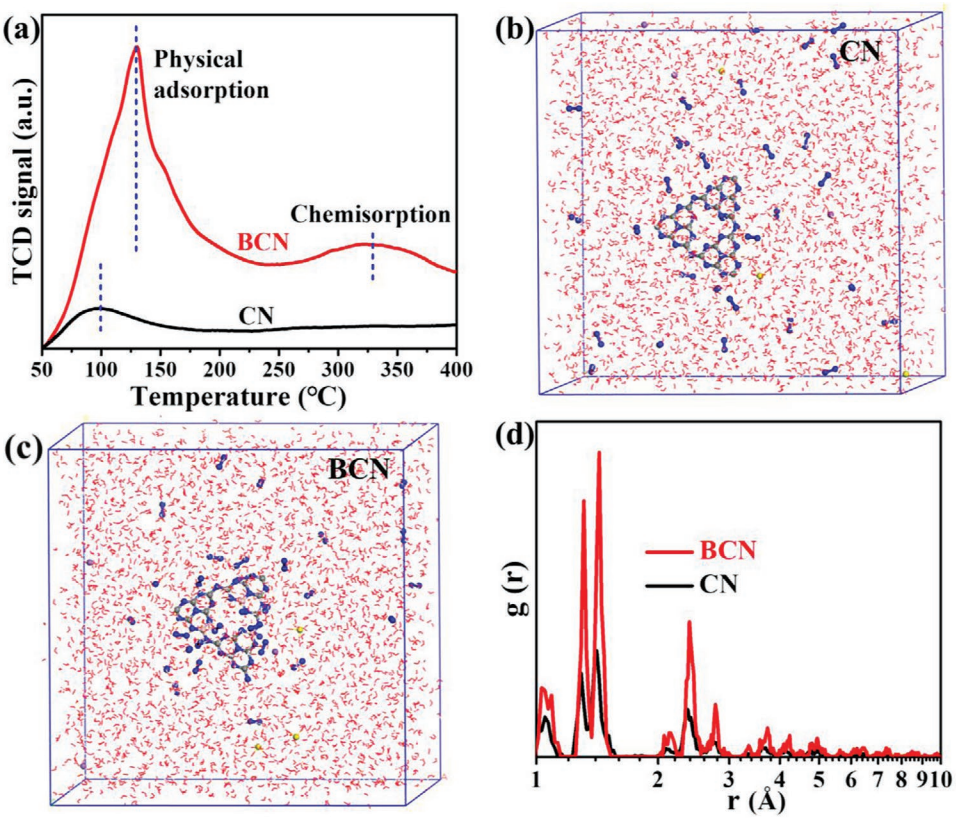

Figure 5. a) N_2-TPD curves, and b,c) MD simulation snapshots of CN and BCN. d) Comparison of RDF for CN and BCN.

BCN under photocatalytic NRR condition (with H_2O, N_2, and Na_2SO_3). It can be clearly noted that the N_2 molecules tend to aggregate more compactly around BCN model, particularly around B-sites, compared with that for CN. Additionally, the radial distribution function (RDF, Figure 5d) was calculated to illustrate the distance from N_2 molecules to photocatalysts. The enhanced $g(r)$ values of RDF for BCN suggest stronger N_2 affinity to B-doping sites compared with those of CN at same radial distance (r). As a consequence, a localized high N_2 concentration around BCN photocatalyst would significantly benefit the reactant N_2 diffusion to the active sites, thus improving the photocatalytic NRR performance.

In this work, the doping of B atoms has been experimentally validated to be highly effective for stabilizing the exposed N atoms in g-C_3N_4, and concurrently improving the visible-light utilization efficiency and decreasing the recombination of photogenerated carriers in g-C_3N_4. Moreover, the excellent porous structure and large surface area of BCN are highly favorable for the exposure of B (or B—N pairs) active sites for the adsorption and activation of N_2 molecules, thus leading to a high photocatalytic NRR performance. However, the NH_3 synthesis mechanism should be very different for the CN and BCN catalysts. With visible-light irradiation, the photogenerated holes in CN or BCN catalyst can be rapidly consumed by the SO_3^{2-} sacrificial agent in solution, and the photogenerated electrons/active *H atoms from water reduction will attack the exposed N atoms in CN to form NH_3 and concurrently generate N vacancies as the catalytic active sites for N_2 adsorption and activation,[37,44,45] while the photogenerated electrons/active *H atoms will attack the active $*N_2$ molecules adsorbed on B (or B—N pairs) active sites to realize the hydrogenation process of N_2. On one hand, our work experimentally validates that the surface exposed active N atoms in g-C_3N_4 can contribute the NH_3 synthesis during the photocatalytic NRR; on the other hand, our work demonstrates that these exposed N atoms in g-C_3N_4 can be firmly stabilized by B-doping to form B—N—C bonds, providing new catalytic active sites for high-efficient NRR to NH_3, experimentally supporting the reported theoretical prediction results.[5,40,41]

3. Conclusion

In summary, the BCN nanosheets were successfully fabricated by a facile thermal treatment approach. The BCN with high B-doping content, good porous structure, and high surface area has been experimentally verified to possess high photocatalytic NRR activity with an NH_3 yield rate of 313.9 μmol g^{-1} h^{-1}. Our study would be helpful for designing and developing high-efficiency metal-free NRR photocatalysts by means of doping approach.

4. Experimental Section

Materials and Chemicals: DICY, B_2O_3, anhydrous sodium sulfite (Na_2SO_3), sodium sulfate (Na_2SO_4), ammonium sulfate ($(^{14}NH_4)_2SO_4$, and deuterium oxide (D_2O) were purchased from Aladdin Ltd (A.R grade). The ^{15}N isotope-labeled ammonium sulfate ($(^{15}NH_4)_2SO_4$ was provided by Shanghai Chemical Research Institute Co. Ltd. (enrichment: 99%).

The N_2 gas (ultrahigh-grade purity, 99.999%), $^{15}N_2$ gas (^{15}N enrichment of 99%), and Ar gas (ultrahigh-grade purity, 99.999%) were supplied from Hefei Ninte gas management co. All materials and chemicals were used as received in the experiment without further purification. DI (18.2 MΩ) water was used during all experiments.

Synthesis of Photocatalysts: In a typical procedure, 5.0 g of DICY was mixed with 0.5 g of B_2O_3 and ground evenly in an agate mortar. Then, the mixture was placed in a crucible with a cover and heated to 600 °C for 3 h in air atmosphere (heating rate of 5 °C min^{-1}) in a muffle furnace. After the crucible was cooled to room temperature, the resultant boron-doped g-C_3N_4 was collected and ground into powder. After that, 0.5 g of as-fabricated boron-doped g-C_3N_4 was thermally treated at 550 °C for 2 h in air with a ramp rate of 5 °C min^{-1} to obtain porous BCN nanosheets product. For meaningful comparison, the pristine g-C_3N_4 nanosheets (CN) sample was also synthesized following the same fabrication procedure except for the absence of B_2O_3 in the synthesis process.

Characterization: The crystalline structures of the samples were recorded by the XRD (Philips X'pert PRO) patterns. The FT-IR spectra were determined on a Perkin-Elmer TGA 7 infrared spectrometer to identify the functional groups on surface of the obtained samples. The morphological observation of both samples was performed on an FE-SEM (SU 8020). The TEM images of the samples were obtained on a JEOL-2010 microscope (Japan). The XPS analysis was recorded on an America ESCALAB 250 X-ray photoelectron spectrometer (Thermo) with Al Kα monochromatized radiations at 1486.6 eV. The UV–vis DRS of the samples were measured on a Japan Shimadzu UV–vis spectrophotometer (UV-2700). The PL spectra of the samples were measured on a FluoroMax-4 spectrofluorometer (Horiba Jobin Yvon, room temperature). All electrochemical measurements were conducted on an electrochemical workstation (CHI660C, China) using a standard three-electrode system with the as-prepared samples coated on F-doped SnO_2-coated glass (FTO) substrate as the working electrode, a Pt mesh (1.5 × 1.5 cm^2) as the counter electrode, and a Ag/AgCl (saturated KCl) as the reference electrode. A 250 W Xe light was utilized as the light source with 0.1 M aqueous Na_2SO_4 solution as the electrolyte. The working electrodes were prepared as follows: 0.05 g of photocatalyst was ground with 0.5 mL of ethanol to form catalyst ink. The catalyst ink was then coated onto a 2 × 1.5 cm^2 of FTO glass) electrode by the doctor blade technique. Next, these electrodes were dried in an oven at 80 °C for 4 h. All investigated electrodes have a similar film thickness of ≈11 µm. The room-temperature electron paramagnetic resonance (ESR) spectra of both CN and BCN powder were recorded by a JES-FA200 ESR spectrometer (JEOL, Japan). The microwave power employed in this work was 1 mW; sweep width ranged from 330 to 345 mT. The chromatograms of possible NO_2– and NO_3– in the NOx detection were conducted by an ion chromatography (IC 6000, Wayeal Co., Ltd, China).

Photocatalytic NRR Experiments: Typically, 20 mg of photocatalyst was first dispersed in 40 mL of aqueous Na_2SO_3 solution (1.0×10^{-3} M, as the photogenerated hole sacrificial agent) in a photocatalytic reactor (CEL-HPR100S+, CeauLight Co. Ltd.), as shown in Figure S6 (Supporting Information). The above mixture was ultrasonically treated to form uniform catalyst suspension solution. And then high purity N_2 was bubbled (30 mL min^{-1}) through the suspension solution under stirring for 30 min in the dark. During light irradiation (with cut-off filter, $\lambda > 400$ nm, light intensity of 0.5 W cm^{-2}, 250 W Xe lamp), 10 mL of sample was taken out of from reactor after 1 h for NH_4^+ concentration analysis. The concentration of NH_4^+ was tested via a colorimetric method using Nessler's reagent (absorbance at 420 nm) via a UV-2700 spectrometer and the corresponding calibration curves are listed in Figure S8 (Supporting Information).[46] In a typical run, 10 mL of the sample was filtered through a membrane (0.22 mm) and placed into a 10 mL of colorimeter tube. Then, 100 µL of potassium sodium tartrate solution was added into the colorimeter tube. After blending, 150 µL of Nessler's reagent was added to the sample tube and mixed. Then, the mixture was aged for 10 min and tested by the UV-2700 spectrometer. The photocatalytic NRR test of each catalyst was repeated for three times. In addition, the long-term and recycling stability measurements were conducted with 40 mg of BCN photocatalyst under the same light irradiation and N_2-saturated condition, as revealed in Figure S14 (Supporting Information). The NH_4^+ concentrations by both photocatalysts were measured after 2, 4, or 6 h under light irradiation, while the recycling stability measurement of the BCN was measured after photocatalytic reaction for 1 h, and then collected, washed, and dried for reuse in next run. Moreover, the corresponding QE of photocatalytic NH_3 synthesis by BCN at different wavelengths was determined using monochromatic filters (CEL-QD420, 450, 500, 550, 600, and 650, CeauLight Co. Ltd.) with a bandwidth of ± 3.0 nm, and calculated as follows:

$$QE = (3 \times [NH_4^+])/(\text{number of incident photons}) \times 100\% \quad ([NH_4^+] \text{ refers to number of } NH_4^+ \text{ product}). \tag{1}$$

NMR Spectra Detection: The ^1H NMR spectra (using superconducting Fourier-transform nuclear magnetic resonance spectrometer, Bruker Avance-400) was applied to detect the trace amount of NH_4^+ under dark condition or Ar bubbling with irradiation. In a typical process, 40 mg of CN and BCN photocatalyst were mixed in 40 mL of Na_2SO_3 (1.0×10^{-3} M) solution and placed in dark condition for 12 h. Then, 10 mL of suspension was taken out through a 0.22 mm membrane and acidized to pH = 2.0 with 0.05 M dilute H_2SO_4. The acidized liquid was concentrated to volume of 1.0 mL at 80 °C in an oven for ^1H NMR measurement (denoted as dark condition in Figure 4a). Similarly, 40 mg of photocatalysts mixed in Na_2SO_3 solution were under light irradiation for 3 h with Ar bubbling (irradiation, Ar bubbling in Figure 4a). In addition, the isotope labeling experiment was carried out by light irradiation for 2 h with 40 mg of BCN photocatalyst using $^{15}N_2$ or $^{14}N_2$ feeding gas.

All the sampling and treatment process were similar to the foremost sample (dark condition). Then, 0.8 mL of concentrated electrolyte was mixed with 0.2 mL of D_2O for ^1H NMR measurements.[39] The ^1H NMR spectra results are illustrated in Figure 4.

Molecular Dynamics Simulations: The MD simulations were realized with Materials Studio (v7.0). The photocatalyst models were immersed in Na_2SO_3/N_2 solution, which was composed of 6 Na^+, 3 SO_3^{2-}, and 60 N_2 molecules and 2000 water molecules under condition of 298 K and 10^{-4} Gpa. The initial state of both models for CN and BCN were illustrated in Figure S15 in the Supporting Information. The simulation time step is 1 femtosecond (fs) and the total simulation time is 50 picoseconds (ps).

Supporting Information

Supporting Information is available from the Wiley Online Library or from the author.

Acknowledgements

W.W. and H.Z. contributed equally to this work. This work was financially supported by the National Natural Science Foundation of China (grant nos 51872292 and 51432009) and the CAS/SAFEA International Partnership Program for Creative Research Teams of Chinese Academy of Sciences, China.

Conflict of Interest

The authors declare no conflict of interest.

Keywords

active N atoms, ammonia synthesis, B—N—C coordination, boron-doped g-C_3N_4, N_2 reduction, photocatalytic nitrogen reduction reaction (NRR)

Received: November 25, 2019
Revised: January 17, 2020
Published online: February 20, 2020

[1] C. Guo, J. Ran, A. Vasileff, S. Z. Qiao, *Energy Environ. Sci.* **2018**, *11*, 45.
[2] X. Wu, L. Xia, Y. Wang, W. Lu, Q. Liu, X. Shi, X. Sun, *Small* **2018**, *14*, 1803111.
[3] a) H. Li, J. Shang, Z. Ai, L. Zhang, *J. Am. Chem. Soc.* **2015**, *137*, 6393; b) T. Wu, X. Zhu, Z. Xing, S. Mou, C. Li, Y. Qiao, Q. Liu, Y. Luo, X. Shi, Y. Zhang, X. P. Sun, *Angew. Chem.* **2019**, *131*, 18620.
[4] M. Li, H. Huang, J. Low, C. Gao, R. Long, Y. Xiong, *Small Methods* **2018**, *3*, 1800388.
[5] C. Ling, X. Niu, Q. Li, A. Du, J. Wang, *J. Am. Chem. Soc.* **2018**, *140*, 14161.
[6] a) Y. Zhao, Y. Zhao, R. Shi, B. Wang, G. I. Waterhouse, L. Z. Wu, C. H. Tung, T. Zhang, *Adv. Mater.* **2019**, *31*, 1806482; b) J. Zhao, B. Wang, Q. Zhou, H. Wang, X. Li, H. Chen, Q. Wei, D. Wu, Y. Luo, J. You, F. Gong, X. P. Sun, *Chem. Commun.* **2019**, *55*, 4997.
[7] P. Qiu, C. Xu, N. Zhou, H. Chen, F. Jiang, *Appl. Catal., B* **2018**, *221*, 27.
[8] a) C. Chen, D. Yan, Y. Wang, Y. Zhou, Y. Zou, Y. Li, S. Wang, *Small* **2019**, *15*, 1805029; b) Y. Zhang, H. Du, Y. Ma, L. Ji, H. Guo, Z. Tian, H. Chen, H. Huang, G. Cui, A. M. Asiri, F. Qu, L. Chen, X. P. Sun, *Nano Res.* **2019**, *12*, 919.
[9] Q. Liu, L. Ai, J. Jiang, *J. Mater. Chem. A* **2018**, *6*, 4102.
[10] M. Ali, F. Zhou, K. Chen, C. Kotzur, C. Xiao, L. Bourgeois, X. Zhang, D. R. Macfarlane, *Nat. Commun.* **2016**, *7*, 11335.
[11] J. Zheng, Y. Lyu, M. Qiao, R. Wang, Y. Zhou, H. Li, C. Chen, Y. Li, H. Zhou, S. P. Jiang, *Chem* **2019**, *5*, 617.
[12] S. Wang, X. Hai, X. Ding, K. Chang, Y. Xiang, X. Meng, Z. Yang, H. Chen, J. Ye, *Adv. Mater.* **2017**, *29*, 1701774.
[13] J. Fu, B. Zhu, C. Jiang, B. Cheng, W. You, J. Yu, *Small* **2017**, *13*, 1603938.
[14] C. Xiao, L. Zhang, K. Wang, H. Wang, Y. Zhou, W. Wang, *Appl. Catal., B* **2018**, *239*, 260.
[15] W. Wang, H. Zhang, S. Zhang, Y. Liu, G. Wang, C. Sun, H. Zhao, *Angew. Chem., Int. Ed.* **2019**, *58*, 2.
[16] D. Xu, B. Cheng, W. Wang, C. Jiang, J. Yu, *Appl. Catal., B* **2018**, *231*, 368.
[17] Y. Shiraishi, S. Shiota, Y. Kofuji, M. Hashimoto, K. Chishiro, H. Hirakawa, S. Tanaka, S. Ichikawa, T. Hirai, *ACS Appl. Energy Mater.* **2018**, *1*, 4169.
[18] M.-A. Légaré, G. Bélanger-Chabot, R. D. Dewhurst, E. Welz, I. Krummenacher, B. Engels, H. Braunschweig, *Science* **2018**, *359*, 896.
[19] L. K. Putri, B.-J. Ng, W.-J. Ong, H. W. Lee, W. S. Chang, S.-P. Chai, *J. Mater. Chem. A* **2018**, *6*, 3181.
[20] N. Sagara, S. Kamimura, T. Tsubota, T. Ohno, *Appl. Catal., B* **2016**, *192*, 193.
[21] S. Cao, J. Low, J. Yu, M. Jaroniec, *Adv. Mater.* **2015**, *27*, 2150.
[22] L. Shi, L. Yang, W. Zhou, Y. Liu, L. Yin, X. Hai, H. Song, J. Ye, *Small* **2018**, *14*, 1703142.
[23] W. Wang, D. Xu, B. Cheng, J. Yu, C. Jiang, *J. Mater. Chem. A* **2017**, *5*, 5020.
[24] P. Xia, B. Zhu, J. Yu, S. Cao, M. Jaroniec, *J. Mater. Chem. A* **2017**, *5*, 3230.
[25] Y. Wang, H. Li, J. Yao, X. Wang, M. Antonietti, *Chem. Sci.* **2011**, *2*, 446.
[26] Z. Lin, X. Wang, *Angew. Chem., Int. Ed.* **2013**, *52*, 1735.
[27] C. Tang, Y. Bando, Y. Huang, C. Zhi, D. Golberg, *Adv. Funct. Mater.* **2008**, *18*, 3653.
[28] W. Lei, D. Portehault, R. Dimova, M. Antonietti, *J. Am. Chem. Soc.* **2011**, *133*, 7121.
[29] C. Huang, C. Chen, M. Zhang, L. Lin, X. Ye, S. Lin, M. Antonietti, X. Wang, *Nat. Commun.* **2015**, *6*, 7698.
[30] Y. Wang, K. Jia, Q. Pan, Y. Xu, Q. Liu, G. Cui, X. Guo, X. Sun, *ACS Sustainable Chem. Eng.* **2018**, *7*, 117.
[31] J. Zhu, T. Diao, W. Wang, X. Xu, X. Sun, S. A. C. Carabineiro, Z. Zhen, *Appl. Catal., B* **2017**, *219*, 92.
[32] G. Liu, G. Zhao, W. Zhou, Y. Liu, H. Pang, H. Zhang, D. Hao, X. Meng, P. Li, T. Kako, *Adv. Funct. Mater.* **2016**, *26*, 6822.
[33] Z. Lian, M. Sakamoto, J. J. Vequizo, C. K. Ranasinghe, A. Yamakata, T. Nagai, K. Kimoto, Y. Kobayashi, N. Tamai, T. Teranishi, *J. Am. Chem. Soc.* **2018**, *141*, 2446.
[34] C. Lv, Y. Qian, C. Yan, Y. Ding, Y. Liu, G. Chen, G. Yu, *Angew. Chem., Int. Ed.* **2018**, *57*, 10246.
[35] a) B. Shen, Y. Chun, J. H. Zhu, Y. Wang, Z. Wu, J. Xia, Q. Xu, *PhysChemComm.* **1999**, *2*, 9; b) Q. Wang, Y. Cao, H. Zeng, Y. Liang, J. Ma, X. Lu, *Chem. Eng. J.* **2019**, *378*, 122143.
[36] N. Zhang, A. Jalil, D. Wu, S. Chen, Y. Liu, C. Gao, W. Ye, Z. Qi, H. Ju, C. Wang, *J. Am. Chem. Soc.* **2018**, *140*, 9434.
[37] G. Dong, W. Ho, C. Wang, *J. Mater. Chem. A* **2015**, *3*, 23435.
[38] a) S. Z. Andersen, V. čolić, S. Yang, J. A. Schwalbe, A. C. Nielander, J. M. Mcenaney, K. Enemark-Rasmussen, J. G. Baker, A. R. Singh, B. A. Rohr, *Nature* **2019**, *570*, 504; b) B. Suryanto, H. Du, D. Wang, J. Chen, A. N. Simonov, D. R. MacFarlane, *Nat. Catal.* **2019**, *2*, 290.
[39] Y. Liu, M. Han, Q. Xiong, S. Zhang, C. Zhao, W. Gong, G. Wang, H. Zhang, H. Zhao, *Adv. Energy Mater.* **2019**, *9*, 1803935.
[40] X. Lv, W. Wei, F. Li, B. Huang, Y. Dai, *Nano Lett.* **2019**, *19*, 6391.
[41] S. Ji, Z. Wang, J. Zhao, *J. Mater. Chem. A* **2019**, *7*, 2392.
[42] X. Yu, P. Han, Z. Wei, L. Huang, Z. Gu, S. Peng, J. Ma, G. Zheng, *Joule* **2018**, *2*, 1610.
[43] S. Liu, M. Wang, T. Qian, H. Ji, J. Liu, C. Yan, *Nat. Commun.* **2019**, *10*, 3898.
[44] X. Li, X. Sun, L. Zhang, S. Sun, W. Wang, *J. Mater. Chem. A* **2018**, *6*, 3005.
[45] B. Hu, M. Hu, L. C. Seefeldt, T. L. Liu, *ACS Energy Lett.* **2019**, *4*, 105.
[46] R. H. Leonard, *Clin. Chem.* **1963**, *12*, 417.